

1 **Morphological Cell Profiling of SARS-CoV-2 Infection Identifies Drug Repurposing**
2 **Candidates for COVID-19**

3 Carmen Mirabelli^{1,*}, Jesse W. Wotring^{2,*}, Charles J. Zhang^{2,†}, Sean M. McCarty^{2,†}, Reid
4 Fursmidt^{3,4,†}, Tristan Frum⁵, Namrata S. Kadambi³, Anya T. Amin³, Teresa R. O'Meara¹, Carla D.
5 Pretto¹, Jason R. Spence^{3,5}, Jessie Huang^{6,7}, Konstantinos D. Alysandratos^{6,7}, Darrell N. Kotton^{6,7},
6 Samuel K. Handelman^{3,4}, Christiane E. Wobus¹, Kevin J. Weatherwax^{4,8,9}, George A.
7 Mashour^{4,8,10}, Matthew J. O'Meara¹¹, Jonathan Z. Sexton^{2,3,4,8}

8 ¹Department of Microbiology and Immunology, University of Michigan Medical School, Ann Arbor,
9 MI, 48109, USA

10 ²Department of Medicinal Chemistry, College of Pharmacy, University of Michigan, Ann Arbor, MI,
11 48109, USA

12 ³Department of Internal Medicine, Gastroenterology, Michigan Medicine at the University of
13 Michigan, Ann Arbor, MI, 48109, USA

14 ⁴U-M Center for Drug Repurposing, University of Michigan, Ann Arbor, MI, 48109, USA

15 ⁵Department of Cell and Developmental Biology, University of Michigan, Ann Arbor, MI, 48109,
16 USA

17 ⁶Center for Regenerative Medicine of Boston University and Boston Medical Center, Boston, MA,
18 02118, USA

19 ⁷The Pulmonary Center and Department of Medicine, Boston University School of Medicine,
20 Boston, MA, 02118, USA

21 ⁸Michigan Institute for Clinical and Health Research (MICHHR), University of Michigan, Ann Arbor,
22 MI, 48109, USA

23 ⁹College of Pharmacy, University of Michigan, Ann Arbor, MI 48109, USA

24 ¹⁰Department of Anesthesiology, Michigan Medicine at the University of Michigan, Ann Arbor, MI,
25 48109, USA

26 ¹¹Department of Computational Medicine and Bioinformatics, University of Michigan, Ann Arbor,
27 MI, 48109, USA

28 *These authors contributed equally to this work.

29 †These authors contributed equally to this work.

30

31 **Abbreviations:**

32 MOI: multiplicity of infection

33 UMAP: uniform manifold approximation and projection

34 COVID-19: Coronavirus Disease-2019

35 MOA: mechanism of action

36 ROI: region of interest

37 iAEC2: induced pluripotent stem cell (iPSC)-derived alveolar epithelial type 2 cells

38 HCQ: hydroxychloroquine

39

40 **Conflicts of interest**

41 The authors declare no conflicts of interest.

42

43

44 **ABSTRACT**

45 The global spread of the severe acute respiratory syndrome coronavirus 2 (SARS-CoV-2), and
46 the associated disease COVID-19, requires therapeutic interventions that can be rapidly
47 translated to clinical care. Unfortunately, traditional drug discovery methods have a >90% failure
48 rate and can take 10-15 years from target identification to clinical use. In contrast, drug
49 repurposing can significantly accelerate translation. We developed a quantitative high-throughput
50 screen to identify efficacious single agents and combination therapies against SARS-CoV-2.
51 Quantitative high-content morphological profiling was coupled with an AI-based machine learning
52 strategy to classify features of cells for infection and stress. This assay detected multiple antiviral
53 mechanisms of action (MOA), including inhibition of viral entry, propagation, and modulation of
54 host cellular responses. From a library of 1,425 FDA-approved compounds and clinical
55 candidates, we identified 16 dose-responsive compounds with antiviral effects. In particular, we
56 discovered that lactoferrin is an effective inhibitor of SARS-CoV-2 infection with an IC_{50} of 308 nM
57 and that it potentiates the efficacy of both remdesivir and hydroxychloroquine. Lactoferrin also
58 stimulates an antiviral host cell response and retains inhibitory activity in iPSC-derived alveolar
59 epithelial cells, a model for the primary site of infection. Given its safety profile in humans, these
60 data suggest that lactoferrin is a readily translatable therapeutic adjunct for COVID-19.
61 Additionally, several commonly prescribed drugs were found to exacerbate viral infection and
62 warrant clinical investigation. We conclude that morphological profiling for drug repurposing is an
63 effective strategy for the selection and optimization of drugs and drug combinations as viable
64 therapeutic options for COVID-19 pandemic and other emerging infectious diseases.

65

66

67

68

69

70 **MAIN**

71 SARS-CoV-2 is an enveloped, positive-sense, single-stranded RNA betacoronavirus that
72 emerged in Wuhan, China in November 2019 and rapidly developed into a global pandemic. The
73 associated disease, COVID-19, has an array of symptoms, ranging from flu-like illness and
74 gastrointestinal distress^{1,2} to acute respiratory distress syndrome, heart arrhythmias, strokes, and
75 death^{3,4}. Drug repurposing has played an important role in the search for COVID-19 therapies.
76 Recently, the FDA issued emergency approval of remdesivir, a nucleoside inhibitor prodrug
77 developed for Ebola virus treatment⁵, and hydroxychloroquine, an aminoquinoline derivative first
78 developed in the 1940s for the treatment of malaria, for patients with severe COVID-19. However,
79 there are no established prophylactic strategies or direct antiviral treatments available to limit
80 SARS-CoV-2 infections and to prevent/cure the associated disease COVID-19.

81

82 Repurposing of FDA-approved drugs is a promising strategy for identifying rapidly deployable
83 treatments for COVID-19. Benefits of repurposing include known safety profiles, robust supply
84 chains, and a short time-frame necessary for development⁶. Additionally, approved drugs serve
85 as chemical probes to understand the biology of viral infection and can make new associations
86 between COVID-19 and molecular targets/pathways that influence pathogenesis of the disease.
87 A complementary approach to standard *in vitro* antiviral assays is high-content imaging-based
88 morphological cell profiling. Using morphological cell profiling, it is possible to identify pathways
89 and novel biology underlying infection, thus allowing for targeted screening around a particular
90 biological process or targeting of host processes that limit viral infection. This enables the
91 identification of multiple anti-viral mechanisms, allowing for the rational design of drug
92 combinations or, conversely, revealing drugs that exacerbate infectivity or are associated with
93 cytotoxicity.

94

95 Here, we developed a pipeline for quantitative high-throughput image-based screening of SARS-
96 CoV-2 infection. We leveraged machine learning approaches to create an assay metric that
97 accurately and robustly identifies features that predict antiviral efficacy and mechanism of action
98 (MOA). We identified several FDA-approved drugs and clinical candidates with unique antiviral
99 activity. We further demonstrated that lactoferrin inhibits viral entry and replication, enhances
100 antiviral host cell response, and potentiates the effects of remdesivir and hydroxychloroquine.
101 Furthermore, we identified currently prescribed drugs that exacerbate viral infectivity. As a
102 confirmatory step, efficacy of lead drugs was validated in a highly physiologically relevant
103 organotypic and biomimetic human model system for bronchial epithelium. Collectively, we
104 present evidence that morphological profiling can robustly identify new potential therapeutics
105 against SARS-CoV-2 infection as well as drugs that potentially worsen COVID-19 outcomes.

106

107 **Morphological profiling reveals unique features associated with SARS-CoV-2 infection**

108 To determine the optimal cell line and appropriate endpoint for antiviral drug screening, we
109 assessed SARS-CoV-2 infectivity in previously reported permissive cell lines: Vero E6, Caco-2,
110 and Huh7⁷. Viral growth kinetics at a multiplicity of infection (MOI) of 0.2 revealed that Vero E6,
111 Caco-2, and Huh7 cells supported viral infection, with peak viral titers at 48 hours post infection
112 (hrs p.i.) (Supplementary Figure 1a/b). Although the viral load was higher in Vero E6 cells, Huh7
113 were selected for our morphological drug screen as a human cell line that expresses both ACE2
114 and TMPRSS2, which are the primary entry factors for SARS-CoV-2⁸. Infection was detectable in
115 Huh7 cells at an MOI as low as 0.004 at 48 hrs p.i. (Supplementary Figure 1c), which highlights
116 the high sensitivity of image-based screening. To identify compounds that inhibit or exacerbate
117 infection, we selected an MOI of 0.2, leading to a baseline infectivity rate of 20%.

118

119 Morphological cell profiling was enabled through multiplexed staining and automated high-content
120 fluorescence microscopy. Our multiplexed dye set included markers for SARS-CoV-2
121 nucleocapsid protein (NP), nuclei (Hoechst 33342), neutral lipids (HCS LipidTox Green), and cell
122 boundaries (HCS CellMask Orange). These fluorescent probes were chosen to capture a wide
123 variety of cellular features relevant to viral infectivity, including nuclear morphology, nuclear
124 texture, cytoplasmic and cytoskeletal features, and indicators of cell health. From initial profiling,
125 we observed three prominent morphological features associated with SARS-CoV-2 infection: the
126 formation of syncytia, increased nucleoli count (Supplementary Figure 1d), and cytoplasmic
127 protrusions (Figure 1). These features, which are key indicators of SARS-CoV-2 infection in Huh7,
128 were used to generate our machine learning pipeline for antiviral drug discovery.

129

130 **Machine learning identifies FDA-approved molecules with antiviral activity against SARS-** 131 **CoV-2**

132 To identify compounds with antiviral activity against SARS-CoV-2, we screened a library of 1,425
133 FDA-approved compounds and rationally included clinical candidates (Supplementary File 1) in
134 quantitative high-throughput screening (qHTS) at five concentrations (50 nM, 250 nM, 500 nM,
135 1000 nM and 2000 nM) in Huh7 cells. Compounds were assessed for their antiviral activity using
136 a CellProfiler-based image analysis pipeline and a random forest classification algorithm to
137 identify infected cells and quantify their morphological characteristics (Figure 2a). The random
138 forest classifier leveraged 660 unique cellular features including measurements of intensity,
139 texture and radial distribution for each fluorescent channel (nuclei, cytoplasm, lipid, virus). From
140 the qHTS, we identified 132 drugs as active with consistent decreases in viral infectivity in at least
141 three of the tested concentrations as well as minimal cytotoxicity.

142

143 In confirmatory screening, 10-point, two-fold dilution dose-response experiments were performed
144 in triplicate on the 132 qHTS hits, with validation of dose-responsive efficacy for 16 compounds
145 below 1 μ M potency (Supplementary Table 1 and Figure 2b). These hits include eleven that are
146 novel *in vitro* observations (bosutinib, domperidone, entecavir, fedratinib, ipratropium bromide,
147 lacoferin, lomitapide, metoclopramide, S1RA, thioguanine, and Z-FA-FMK), and six that have
148 been previously identified to have antiviral activity (amiodarone, verapamil, gilteritinib,
149 clofazimine^{9,10}, niclosamide¹¹, and remdesivir). Amiodarone, gilteritinib, lomitapide, thioguanidine
150 and Z-FA-FMK retained activity in a traditional CPE-based antiviral assay in Vero E6
151 (Supplementary Table 1). In addition to antiviral drug hits, we also identified several compounds
152 that appear to exacerbate SARS-CoV-2 infection, including trametinib, binimetinib and
153 cobimetinib -potent MEK inhibitors used to treat metastatic melanoma- and the Parkinson's
154 disease drugs carbidopa, methyldopa and levodopa (Supplementary Figure 2).

155

156 **Cell level feature clustering reveals potential mechanisms of action for lead compounds**

157 In contrast to standard single-endpoint *in vitro* assays, morphological cell profiling allows for the
158 efficient visualization and quantitation of biological characteristics of viral infection and cytotoxicity.
159 To assist with mechanistic determination, 379 representative cellular features were dimensionality
160 reduced via the non-linear uniform manifold approximation and projection (UMAP) to embed for
161 1.96 million cells into 2-dimensions to plot clusters of cells based on their distinct morphological
162 features¹². Then we re-embed 18.9 million cells from 15 plates to observe the perturbation of
163 feature distributions through a range of drug concentrations relative to negative and positive
164 controls (Figure 2, Supplementary Figure 3b).

165

166 In the UMAP embedding, we identified 15 regions of interest (ROI) with high cell density (Figure
167 3b). A broad density region (ROIs 10,15) contained 8.4 million uninfected cells with satellite
168 populations having characteristic morphologies including 0.59 million undergoing cell division
169 (ROI 6) and 1.09 million accumulating of lipids towards the periphery of the cell (ROI 12). A large
170 disconnected region (ROIs 1-4) contained 85 thousand isolated infected cells (ROI 4), 0.43 million
171 infected cells in syncytia (ROI 3), and 1.3 million cells adjacent to infected cells (ROIs 1,2) (Figure
172 3c). Pseudotime of the viral infection progression can be inferred through inspection of cluster
173 populations where cells begin in the main cluster body (ROIs 10,15) and traverse to the infected
174 cluster (ROIs 1-4) where there is punctate viral signal (ROI 1) which progress to isolated infected
175 cells characterized by homogenous NP staining throughout the cytoplasm (ROI 2), and ends with
176 infection of surrounding cells and the formation of syncytia (ROIs 3,4). All efficacious compounds
177 deplete ROIs 1-4 and thioguanine, clofazimine, S1RA and gilteritinib show differences in the
178 UMAP cluster dynamics (Supplementary Figure 3) suggestive of different MOAs.

179

180 **Lactoferrin blocks SARS-CoV-2 replication at different stages of the viral cycle**

181 One of the most efficacious hits identified from our screen was lactoferrin, a protein found in milk
182 and other secretory fluids¹³. We determined that lactoferrin has dose-dependent antiviral activity
183 through a range of MOIs (Figure 4a and b). Previous work on lactoferrin in the context of infection
184 with SARS-CoV-1 suggests that it blocks viral entry by binding heparan sulfate proteoglycans that
185 are important for early viral attachment¹⁴. Our studies showed that lactoferrin blocks SARS-CoV-
186 2 infection through entry inhibition and is also capable of rescuing infection when added 1 or 24
187 hrs p.i. (Figure 4b). Lactoferrin has been proposed to enhance innate interferon responses to limit
188 viral replication within host cells¹⁵. Upon treatment, we observed a dose-dependent reduction of
189 viral replication (Figure 4c), which was consistent with elevated mRNA levels of IFN β and

190 interferon-stimulated genes (ISG15, MX1, Viperin and IFITM3) in lactoferrin-treated Huh7 cells
191 (Figure 4d). Interestingly, we detected a robust antiviral effect by both holo and apolactoferrin
192 (human and bovine), the latter being the component of widely available dietary supplements. To
193 rule out a mode of action that involved a general iron depletion mechanism, we tested the protein
194 transferrin and found that it was devoid of any anti-SARS-CoV-2 activity at the highest
195 concentration of 2.3 μ M (Figure 4e).

196

197 A clinically effective strategy for antiviral therapies uses a combinatorial (or “drug cocktail”)
198 approach, where compounds with varying MOAs are concomitantly used to target different stages
199 in the viral life cycle and to minimize the risk of drug resistance from single-agent selective
200 pressure. This is especially true for RNA viruses, which are highly variable and can develop drug-
201 resistance¹⁶. Given the pronounced single-agent efficacy of lactoferrin, we tested whether
202 combinations with remdesivir or hydroxychloroquine could improve the overall antiviral activity.
203 We found that lactoferrin potentiates the efficacy of both remdesivir (Figure 4f and Supplementary
204 Figure 4a) and hydroxychloroquine (Figure 4f and Supplementary Figure 4f), which are currently
205 explored treatments for SARS-CoV-2 infection. Therefore, combination therapy with lactoferrin
206 could be beneficial in the management of the COVID-19 pandemic by reducing toxicity (e.g.,
207 hydroxychloroquine) or consumption (e.g., remdesivir).

208

209 **Lead compounds demonstrate efficacy in iPSC-derived model of bronchial epithelium**

210 To evaluate the translatability of our identified lead compounds, we used a biomimetic model of
211 bronchial epithelium, iPSC-derived alveolar epithelial type 2 cells (iAEC2s)¹⁷. Surfactant protein
212 C positive (SFTPC+) epithelial cells were previously used to model other lung diseases in place
213 of primary AEC2s¹⁸. The advantage of using iPSC-derived AEC2s consists in the development of

214 an heterogeneous populations that contains also alveolar type II cells, the latter being involved in
215 COVID-19 pathogenesis¹⁹. We demonstrated that iAECs are amenable to infection with an MOI
216 of 10, resulting in about 50-60% infected cells. Acetylated tubulin staining revealed variable
217 cytoskeleton structures, reminiscent of different cell types, and interesting protrusions that co-
218 stained with viral marker NP. Morphology of infected cells also have key differences as compared
219 to other cell types used in our study; particularly, the proportion of individually infected cells are
220 greater than viral syncytia (Figure 5b). Remarkably, even at a high MOI of 10, dose-responsive
221 antiviral activity was observed with bovine lactoferrin (IC₅₀ = 45 nM), human lactoferrin (IC₅₀ = 466
222 nM), S1RA (IC₅₀ = 1 μM), and remdesivir (IC₅₀ = 18 nM) (Figure 5a). This physiologic relevant
223 model is a proxy of human lung tissue and serves as an intermediate model to further validate
224 clinical potential of our identified lead compounds prior to *in vivo* studies.

225

226 **DISCUSSION**

227 In this study, we developed an experimental workflow based on high-content imaging and
228 morphological profiling that allows for rapid screening of FDA-approved compounds, leveraging
229 machine learning to determine potential MOA. We identified 17 FDA-approved compounds that
230 limit SARS-CoV-2 infection *in vitro*. Of these, six were previously reported and serve as a
231 benchmark validation of our endpoints and experimental approach, and eleven were hitherto
232 unknown. We demonstrate that this approach is versatile (i.e., it can be applied to both
233 transformed and more physiologically-relevant non-transformed cell lines) and can identify the
234 emergent properties of the infection as well as novel phenotypes that can be perturbed through
235 chemical inhibition.

236

237 A high-content morphological cell profiling approach is superior to image cytometry (tabulating
238 percent positive) and plate reader assays for selecting and prioritizing drugs for repurposing. Here,

239 viral staining is not merely an absolute measure for viral infection (or inhibition) but the starting
240 point for a detailed investigation of infection trajectories and observations of numerous phenotypic
241 targets, including inhibition of syncytia formation, viral entry, or viral replication, and modulation
242 of the host cell. We report compounds with strong antiviral activity against SARS-CoV-2 and also
243 their putative MOA.

244
245 The UMAP embedding was highly effective for visualizing the infected cell population and the
246 progression of the viral infection trajectory was clearly visible. We gained insight into the putative
247 antiviral MOAs via inspection of the cluster populations. For thioguanine and clofazimine,
248 increasing concentrations appear to suppress isolated single infected cells (ROI 4) while a small
249 number of syncytia (ROI 3) are still observable (Supplementary Figure 3b), suggesting a
250 replication inhibition MOA. This observation is consistent with the established MOA of both drugs
251 as inhibitors of nucleic acid synthesis^{20,21}. S1RA reduces ROIs 1-4 evenly, but ROI 13 increases
252 (Supplementary Figure 3b: S1RA) and is characterized by increased cytoplasmic nucleic acid
253 staining (Supplementary Figure 3a: ROI 13), suggesting a host-modulation MOA. Lastly,
254 gilteritinib demonstrates an increase in ROI 12 with treatment (Supplementary Figure 3b:
255 gilteritinib), a cell cluster defined by large and distributed lipid accumulation (Supplementary
256 Figure 3a: ROI 12). Lipid accumulation, in liver-derived Huh7 cells, is associated with cytotoxicity
257 and is consistent with reduction in viability with escalating dose (Figure 2b)²².

258
259 Importantly, our study identified drugs that implicate new molecular targets/pathways in the
260 pathogenesis of SARS-CoV-2 and produce clinically testable and readily translatable hypotheses.
261 As an example, we observed dose-dependent antiviral activities of metoclopramide and
262 domperidone, two potent dopamine receptor D2 antagonists used to treat gastroesophageal
263 reflux disease and prevent other gastrointestinal symptoms, including nausea and vomiting²³.
264 Gastrointestinal symptoms have been increasingly reported in more than half of the patients

265 infected by SARS-CoV-2². Notably, investigational drugs like hydroxychloroquine, lopinavir-
266 ritonavir, tocilizumab and others can be associated with gastrointestinal and hepatic adverse
267 events and hence are not ideal for patients already experiencing severe GI symptoms²⁴.
268 Metoclopramide and domperidone therefore represent a dual-target therapeutic option for
269 COVID-19 patients. In contrast, the pro-dopaminergic drugs carbidopa, levodopa, and
270 methyldopa promote infection (Supplementary Figure 2), suggesting that the dopamine pathway
271 may contribute to infection outcomes. Additionally, all of the FDA-approved MEK inhibitors
272 exacerbate viral infection 3-fold indicating a putative role of MEK in SARS-CoV-2 pathogenesis.
273 These *in vitro* observations should be validated through clinical research that examines whether
274 concomitant presence of drug and SARS-CoV-2 infection worsen COVID-19 symptoms.

275

276 As most FDA-approved drugs are optimized against human molecular targets, our screen helped
277 identify crucial host factors involved in SARS-CoV-2 infection. Z-FA-FMK, an irreversible inhibitor
278 of cysteine proteases, including cathepsins B, L, and S²⁵, exhibited potent antiviral activity. A
279 recent report using a pseudovirus indicated cathepsin L is an entry factor of SARS-CoV-2²⁶. The
280 antiviral effect of Z-FA-FMK suggests that cathepsin L is a requirement also in the context of
281 SARS-CoV-2 infection and suggests that this molecule could be a useful investigational tool to
282 study virus entry. Similarly, fedratinib, approved by the FDA in 2019 for myeloproliferative
283 neoplasm²⁷, is an orally bioavailable semi-selective JAK2 inhibitor. JAK-inhibitors have been
284 proposed for COVID-19 to specifically inhibit TH17-mediated inflammatory responses. JAK-
285 inhibitors have been proposed for COVID-19 treatment to specifically inhibit TH17-mediated
286 inflammatory response^{28,29} and to block numb-associated kinase responsible for clathrin-
287 mediated viral endocytosis³⁰. Several JAK-inhibitors are currently evaluated in clinical trials for
288 COVID-19 management, including with baricitinib³¹, jakotinib (ChiCTR2000030170), and
289 ruxolitinib (ChiCTR2000029580). For their inhibitory effect on innate immune response at the

290 cellular level, JAK-inhibitors could serve as useful tools in the future to elucidate the involvement
291 of the innate immune response in SARS-CoV-2 infection.

292

293 The sigma receptors (SigmaR1/R2) are permissive chaperones that mediate endoplasmic
294 reticulum stress response and lipid homeostasis³², processes that have been implicated in early
295 stages of hepatitis C viral infection in Huh7 cells³³ and coronavirus pathogenesis³⁴. We identified
296 two sigma receptor modulators amiodarone³⁵, and S1RA³⁶ with potent antiviral activity,
297 demonstrating IC₅₀ values of 52 nM and 222 nM, respectively, with limited cell toxicity.
298 Amiodarone is approved for treatment of arrhythmias but, like hydroxychloroquine, has potent
299 cardiotoxic side effects through inhibition of the hERG ion channel³⁷ that limit therapeutic potential.
300 S1RA has completed phase II clinical trials for the treatment of neuropathic pain^{38,39}. Although
301 Gordon *et al.* identified several other sigmaR1/R2 modulators that inhibited SARS-CoV-2 infection
302 in Vero-E6 cells, antiviral activity for S1RA was not observed⁴⁰. This suggests that the activity of
303 S1RA is dependent on host cell factors specific to each cell line and, promisingly, that human
304 cells may be more responsive to this compound, as observed in iAEC2s (Figure 5a).

305

306 Most noteworthy, our screen demonstrates lactoferrin as a SARS-CoV-2 inhibitor *in vitro* with
307 multimodal efficacy. We showed dose-dependent efficacy in multiple cell types, including a non-
308 transformed and clinically relevant iPSC-derived model of alveolar epithelium (Figure 4f).
309 Lactoferrin gene expression has been shown previously to be highly upregulated in response to
310 SARS-CoV-1 infection⁴¹ and, in addition to enhancing natural killer cell and neutrophil activity,
311 lactoferrin blocks viral entry through binding to heparan sulfate proteoglycans. Lactoferrin retains
312 anti-SARS-CoV-2 activity 24 hrs p.i., which suggests additional MOA other than simple entry
313 inhibition. Although we cannot conclude a definitive and complete MOA, we show significant host
314 cell modulation through increased expression of several interferon-stimulated genes upon
315 treatment with lactoferrin. Additionally, lactoferrin has been previously shown to decrease the

316 production of IL-6⁴², which is one of the key players of the “cytokine storm” produced by SARS-
317 CoV-2 infection^{43,44}. We found that lactoferrin, either from bovine or human origin, retain activity
318 in both the holo- and apo- forms, the latter being the component of orally available lactoferrin
319 supplements. Lactoferrin potential is heightened by its ability to mitigate a high MOI SARS-CoV-
320 2 infection in iAEC2 (Figure 5). Orally available lactoferrin could be especially effective in resolving
321 the gastrointestinal symptoms that are present in COVID-19 patients⁴⁵. The mechanisms may be
322 similar to how lactoferrin reduces human norovirus infection through induction of innate immune
323 responses⁴⁶, especially as lactoferrin gene polymorphisms are associated with increased
324 susceptibility to infectious diarrhea⁴⁷. If lactoferrin reduces viral load in the GI tract, it could reduce
325 fecal-oral transmission of COVID-19⁴⁸.

326

327 Combination therapies are likely to be required for effectively treating SARS-CoV-2 infection, and
328 this approach has already shown promise. For example, combination therapy with interferon beta-
329 1b, lopinavir–ritonavir, and ribavirin showed efficacy against SARS-CoV-2 in a prospective, open-
330 label, randomized, phase 2 trial⁴⁹. We show that lactoferrin potentiates the antiviral activity of both
331 remdesivir and hydroxychloroquine and could be used as a combination therapy with these drugs,
332 which are currently being used or studied for the treatment of COVID-19. Due to its wide
333 availability, limited cost, and lack of adverse effects, lactoferrin could be a rapidly deployable
334 option for both prophylaxis and the management of COVID-19. Likewise, ipratropium bromide, a
335 widely-used quaternary ammonium salt bronchodilator, holds promise as another agent for
336 combination therapies with potential to reduce bronchial viral burden.

337

338 Although our findings are promising, further studies are needed to confirm their efficacy in other
339 representative *in vitro* cell lines and/or clinical studies. UMAP analysis provides limited insight to
340 MOA and serve as a basis for future pharmacological studies specific to our compounds in
341 treatment of SARS-CoV-2. These studies are currently ongoing.

342

343 High-content morphological cell profiling for drug repurposing screening enabled the identification
344 of both novel antivirals efficacious against SARS-CoV-2 and compounds that possibly exacerbate
345 SARS-CoV-2 infection. Furthermore, in contrast to other drug repurposing studies, the assay
346 reported here allowed for the identification of potential MOA, including host cell responses.
347 Confirmation in iAEC2s suggest high clinical translatability of these compounds. This approach
348 to preclinical testing has promise for identifying other anti-SARS-CoV-2 drugs, rationally designing
349 therapeutic combinations with multiple MOAs, and deployment of optimized combinations in a
350 rapid and systemic fashion.

351

352

353

354

355

356

357

358

359

360

361

362 Supplementary Information is available for this paper.

363

364 Correspondence and requests for materials should be addressed to jzsexton@umich.edu

365

366

367

368

369

370

371 **ACKNOWLEDGEMENTS**

372 Funding: University of Michigan Institute for Clinical and Health Research (MICHR) (NCATS -
373 UL1TR002240) and its Center for Drug Repurposing. JZS is supported by the National Institute
374 of Diabetes and Digestive and Kidney Diseases (R01DK120623). JWW is supported by the
375 pharmacological sciences training program (PSTP) T32 training grant. CM is supported by Marie-
376 Slodowska Curie individual fellowship (GA - 841247) and MICHR Postdoctoral Translational
377 Scholars Program. KDA is supported by the I.M. Rosenzweig Junior Investigator Award from the
378 Pulmonary Fibrosis Foundation. JRS is supported by the National Heart, Lung, and Blood Institute
379 (NHLBI – R01HL119215), by the NIAID Novel Alternative Model Systems for Enteric Diseases
380 (NAMSED) consortium (U19AI116482) and by grant number CZF2019-002440 from the Chan
381 Zuckerberg Initiative DAF, an advised fund of Silicon Valley Community Foundation.

382

383 The authors would like to thank Matthew Chess for Amazon AWS support, Kevin Jan and Peyton
384 Uhl at Yokogawa for imaging support, Nick Santoro at the University of Michigan Center for
385 Chemical Genomics. We thank David Egan and Wienand Omta from Core Life Analytics for
386 assisting high content data analytics as well as Philip Cheung and Brian Bolt at ReFactor
387 Biosciences for assistance with HTS data registration. Finally, we thank Tracey Schultz and
388 Dianne Jazdyk for project management.

389

390 **METHODS**

391 **Cells and virus.** Vero E6, Caco-2 and Huh7 cells were maintained at 37°C with 5% CO₂ in
392 Dulbecco's Modified Eagle's Medium (DMEM; Welgene), supplemented with 10% heat-
393 inactivated fetal bovine serum (FBS), HEPES, non-essential amino-acids, L-glutamine and 1X

394 Antibiotic-Antimycotic solution (Gibco). iPSC (SPC2 iPSC line, clone SPC2-ST-B2, Boston
395 University) derived alveolar epithelial type 2 cells (iAEC2s) were differentiated as previously
396 described and maintained as alveolospheres embedded in 3D Matrigel in "CK+DCI" media, as
397 previously described (Jacob et al. 2019). iAEC2s were passaged approximately every two weeks
398 by dissociation into single cells via the sequential application of dispase (2mg/ml, Thermo Fisher
399 Scientific, 17105-04) and 0.05% trypsin (Invitrogen, 25300054) and re-plated at a density of 400
400 cells/ μ l of Matrigel (Corning, 356231), as previously described (Jacob et al. 2019). SARS-CoV-2
401 WA1 strain was obtained by BEI resources and was propagated in Vero E6 cells. Viral titers were
402 determined by TCID50 assays in Vero E6 cells (Reed and Muench method) by microscopic
403 scoring. All experiments using SARS-CoV-2 were performed at the University of Michigan under
404 Biosafety Level 3 (BSL3) protocols in compliance with containment procedures in laboratories
405 approved for use by the University of Michigan Institutional Biosafety Committee (IBC) and
406 Environment, Health and Safety (EHS).

407

408 **Viral titer determination.** Vero E6, Caco-2 and Huh7 cells were seeded in a 48-well plate at
409 2×10^4 cells/well incubated overnight at 37°C with 5% CO₂. Cells were then infected with SARS-
410 CoV-2 WA1 at a multiplicity of infection (MOI) of 0.2. One hour after infection, cells were harvested
411 (day 0 of infection) or kept at 37°C for 1, 2 and 3 days p.i. Viral titer determination was performed
412 by TCID50 assay on Vero E6 cells of the total virus (supernatant and intracellular fraction).
413 Alternatively, cells were harvested with Trizol and total cellular and viral RNA was extracted with
414 the ZymoGen Direct-zol RNA extraction kit. Viral RNA was quantified by RT-qPCR using the
415 2019-nCoV CDC qPCR Probe Assay and the probe set N1 (IDT technologies). IFN β , viperin, MX1,
416 ISG15, IFITM3 and the housekeeping gene GAPDH mRNA levels were quantified by qPCR with
417 SsoAdvanced™ Universal SYBR® Green Supermix (Bio-Rad) with specific primers (IFN β : F-
418 TTGACATCCCTGAGGAGATTAAGC, R- TCCCACGTACTCCA ACTTCCA; MX1: F-
419 CCAGCTGCTGCATCCCACCC, R-AGGGGCGCACCTT CTCCTCA; ISG15: F-

420 TGGCGGGCAACGAATT, R- GGGTGATCTGCGCCTTCA; IFITM3: F-TCCCAC
421 GTACTCCAACCTTCCA, R-AGCACCAGAAACACGTGCACT; GAPDH: F-
422 CTCTGCTCCTCCTGTTCGAC, R-GCGCCCCACCAAGCTCAAGA). Fold increase was
423 calculated by using the $\Delta\Delta C_t$ method over non-infected untreated Huh7.

424

425 **Viral infectivity assay.** 384-well plates (Perkin Elmer, 6057300) were seeded with Huh7 cells at
426 3000 cells/well and allowed to adhere overnight. Compounds were then added to the cells and
427 incubated for 4 hours. The plates were then transferred to BSL3 containment and infected with
428 SARS-CoV-2 WA1 at a multiplicity of infection (MOI) of 0.2 in a 10 μ L addition with shaking to
429 distribute virus. For the final dose-responses curves, porcine trypsin (Sigma-Aldrich, T0303) at a
430 final concentration of 2 μ g/ml was included during infection. After one hour of absorption, the virus
431 inoculum was removed, and media replaced with fresh compound. Uninfected cells and vehicle-
432 treated cells were included as positive and negative control, respectively. Two days post-infection,
433 cells were fixed with 4% PFA for 30 minutes at room temperature, permeabilized with 0.3% Triton
434 X-100 and blocked with antibody buffer (1.5% BSA, 1% goat serum and 0.0025% Tween 20). The
435 plates were then sealed, surface decontaminated, and transferred to BSL2 for staining with the
436 optimized fluorescent dye-set: anti-nucleocapsid protein (anti-NP) SARS-CoV-2 antibody
437 (Antibodies Online, Cat# ABIN6952432) overnight treatment at 4C followed by staining with
438 secondary antibody Alexa-647 (goat anti-mouse, Thermo Fisher, A21235), Hoechst-33342
439 pentahydrate (bis-benzimide) for nuclei staining (Thermo Fisher, H1398), HCS LipidTOX™ Green
440 Neutral Lipid Stain (Thermo Fisher, H34475), and HCS CellMask™ Orange for cell delineation
441 (Thermo Fisher H32713). iAEC2 maintained in 3D culture were dissociated to single cells and
442 seeded in collagen coated 384-well plates at a seeding density of 8000 cells/well in the presence
443 of 10 μ M Y-27632 for the first 72 hours after plating (APEX BIO, A3008 to grow to roughly 80%
444 confluence. Infection was performed at MOI of 10 in the presence of 2 μ g/ml of trypsin porcine

445 (Sigma-Aldrich, T0303). Staining protocol for the iAEC2s differed slightly with the addition of an
446 anti-acetylated tubulin primary antibody (Cell Signaling, 5335), instead of HCS CellMask Orange,
447 and the use of an additional secondary Alexa 488 antibody (donkey anti-rabbit, Jackson
448 ImmunoResearch, 711-545-152).

449

450 **Multi-cycle cytopathogenic effect (CPE) reduction assay.** Vero E6 were allowed to adhere
451 overnight in 96-well cell culture plates. A 1:2 10-point serial dilution of compounds (5000nM-5nM)
452 and SARS-CoV-2 at MOI of 0.002 were added. CPE was evaluated by microscopic scoring at
453 5dpi. The 50% inhibitory concentration (IC₅₀) was calculated by logarithmic interpolation and is
454 defined as the concentration at which the virus-induced CPE is reduced by 50%.

455

456 **Compound library.** The compound library deployed for drug screening was created using the
457 FDA-Approved Drugs Screening Library (Item No. 23538) from Cayman Chemical Company. This
458 library of 875 compounds was supplemented with additional FDA approved drugs and rationally
459 included clinical candidates from other vendors including MedChemExpress, Sigma Aldrich, and
460 Tocris. Our library was formatted in five 384-well compound plates and was dissolved in DMSO
461 at 10 mM. Hololactoferrin (Sigma Aldrich, L4765), apolactoferrin (Jarrow Formulas, 121011),
462 native human lactoferrin (Creative BioMart, LFT-8196H) and transferrin (Sigma Aldrich, T2036)
463 were handled separately and added manually in cell culture media. Dilution plates were generated
464 for qHTS at concentrations of 2 mM, 1 mM, 500 μ M, 250 μ M and 50 μ M and compounds were
465 dispensed at 1:1000 dilution.

466

467 **qHTS primary screen and 1st sonse confirmation.** For the qHTS screen, compounds were added
468 to cells using a 50 nL pin tool Caliper Life Sciences Sciclone ALH 3000 Advanced Liquid Handling
469 system at the University of Michigan Center for Chemical Genomics (CCG). Concentrations of 2

470 μM , 1 μM , 500 nM, 250 nM and 50 nM were included for the primary screen. Post qHTS screen,
471 all compounds were dispensed using an HP D300e Digital Compound Dispenser and normalized
472 to a final DMSO concentration of 0.1% DMSO. Confirmation dose response was performed in
473 triplicate and in 10-point:2-fold dilution.

474

475 **Imaging.** Stained cell plates were imaged on both Yokogawa CQ1 and Thermo Fisher CX5 high
476 content microscopes with a 20X/0.45NA LUCPlan FLN objective. Yokogawa CQ1 imaging was
477 performed with four excitation laser lines (405nm/488nm/561nm/640nm) with spinning disc
478 confocal and 100ms exposure times. Laser power was adjusted to yield optimal signal to noise
479 ratio for each channel. Maximum intensity projection images were collected from 5 confocal
480 planes with a 3 micron step size. Laser autofocus was performed and nine fields per well were
481 imaged covering approximately 80% of the well area. The Thermofisher CX5 with LED excitation
482 (386/23nm, 485/20nm, 560/25nm, 650/13nm) was also used and exposure times were optimized
483 to maximize signal/background. Nine fields were collected at a single Z-plane as determined by
484 image-based autofocus on the Hoechst channel. The primary qHTS screen was performed using
485 CX5 images and all dose-response plates were imaged using the CQ1.

486

487 **Image segmentation and feature extraction.** The open source CellProfiler software was used
488 in an Ubuntu Linux-based distributed Amazon AWS cloud implementation for segmentation,
489 feature extraction and results were written to an Amazon RDS relational database using MySQL.
490 A pipeline was developed to automatically identify the nuclei, cell, cytoplasm, nucleoli, neutral
491 lipid droplets and syncytia for feature extraction. Multiple intensity features and radial distributions
492 were measured for each object in each channel and cell size and shape features were measured.
493 Nuclei were segmented using the Hoechst-33342 image and the whole cell mask was generated
494 by expanding the nuclear mask to the edge of the Cell Mask Orange image.

495

496 **Data pre-processing.** Cell level data were pre-processed and analyzed in the open source
497 Knime analytics platform⁵⁰. Cell-level data was imported into Knime from MySQL, drug treatment
498 metadata was joined, and features were centered and scaled. Features were pruned for low
499 variance (<5%) and high correlation (>95%) and resulted in 660 features per cell.

500

501 **Statistical methods and hypothesis testing.** Dose-response curves were fit and pairwise
502 differences between experimental conditions were tested using Prism (Graphpad Software,
503 San Diego, CA, USA). Other statistical tests were performed in the statistical programming
504 language and environment R.

505

506 **Machine learning - infectivity score and field-level scoring.** Multiple logistic regression as
507 implemented in the statistical language and environment R was used to identify features
508 characteristic of cells within infected wells. Models were fit to cells from infected and
509 uninfected control wells in the first five plate-series of the quantitative high throughput screen.
510 As an independent benchmark, these logistic regression models were validated against a
511 manually selected set of individual infected and uninfected cells; features which degraded
512 performance on the benchmark were excluded from the model. The final model included only
513 virus channel intensity features in the cell and cytoplasm ROIs. As a threshold for initial
514 classification, the minimum value from virus-infected cells in the benchmark was used; the
515 final decision rule is given in Eq. 1.

516

517 (Eq.1) : A cell is infected if (Cells_Intensity_IntegratedIntensityEdge_Virus × 0.1487025 +
518 Cells_Intensity_MeanIntensityEdge_Virus × -38.40196 +
519 Cells_Intensity_MaxIntensityEdge_Virus × 42.70269 +
520 Cytoplasm_Intensity_StdIntensity_Virus × 42.54849) ≥ 1.525285

521

522 Then, individual field images from the infected control were categorized as confirmed-infected
523 when the mean feature values, across all cells in the field, were above the threshold in Eq. 1.
524 Using mean values for all 660 cell-profiler features in each field, a random forest classifier
525 was trained to predict a probability of membership in the category of uninfected control fields
526 vs confirmed-infected fields. The output of this random forest classifier is reported as
527 “Probpos” (for the positive, uninfected control), throughout. Field level mean/median feature
528 values were computed and a random forest model was fit between the positive control (32
529 uninfected wells) and the negative control (32 infected wells, 0.1% DMSO vehicle treated)
530 with 80/20 cross validation. The compound treated wells were scored with the RF model and
531 the efficacy score was normalized to the individual plate.

532

533 **UMAP embedding.** The embed_umap application of MPLearn (v0.1.0,
534 <https://github.com/momeara/MPLearn>) was used to generate UMAP embeddings. Briefly, each
535 for a set of cells, each feature was per-plate standardized and jointly orthogonalized using
536 sklearn.IncrementalPCA(n_components=379, batch_size=1000). Then features were embedded
537 into 2-dimensions using umap-learn (v0.4.1)¹² with umap. UMAP(n_components=2,
538 n_neighbors=15, min_dist=0, init='spectral', low_memory=True). Embeddings were visualized
539 using Holovies Datashader (v1.12.7)⁵¹, using histogram equalization and the viridis color map.
540 Visualizing subsets was done in JMP Pro 14.

541

542 **Data analytics.** HC Stratominer (Core Life Analytics, Utrecht NL) was used as an independent
543 method for hit-calling and performs fully automated/streamlined cell-level data pre-processing and
544 score generation. IC Stratominer was also used to fit dose response curves for qHTS.
545 Compound registration and assay data registration were performed using the open source
546 ACAS platform (Refactor BioSciences github <https://github.com/RefactorBio/acas>).

547

548 **Dose-response analysis and compound selection.** In qHTS screening, a compound was
549 selected to be carried forward into full dose response confirmation when meeting one of the
550 following criteria: 1) Probpos greater than 0.75 for the median field in at least three concentrations,
551 with per-field cell counts at least 60% of the positive control, and without an observed standard
552 deviation in Probpos across-fields-in-the-well of 0.4 or greater, 2) a dose-response relationship
553 with Probpos was observed (by inspection) across the five concentrations tested, including
554 compounds with Probpos greater than 0.90 at the two highest concentrations, or 3) compounds
555 of interest not meeting this criteria were carried forward if reported positive in the literature or were
556 being evaluated in clinical trials for COVID-19.

557

558 **Dose response analysis in the confirmation and combinatorial screening.** Due to the spatial
559 inhomogeneity of infected cells across a single well, approximately half of the fields were
560 undersaturated, leading to a consistent distribution in Probpos that saturates in the top third of 27
561 rank-ordered fields (from 9 fields and triplicate wells) for each concentration tested. The Probpos
562 effect for a compound concentration was tabulated by averaging the top third of rank ordered
563 fields. Outlier fields with high Probpos values were visually inspected and eliminated if artifacts
564 (segmentation errors or debris) were observed. Cells treated with known fluorescence drugs

565 including Clofazimine, were confirmed to not have spectral interference. Dose response curves
566 were fit with Graphpad Prism using a semilog 4-parameter variable slope model.

567

568

569

570

571

572

573

574

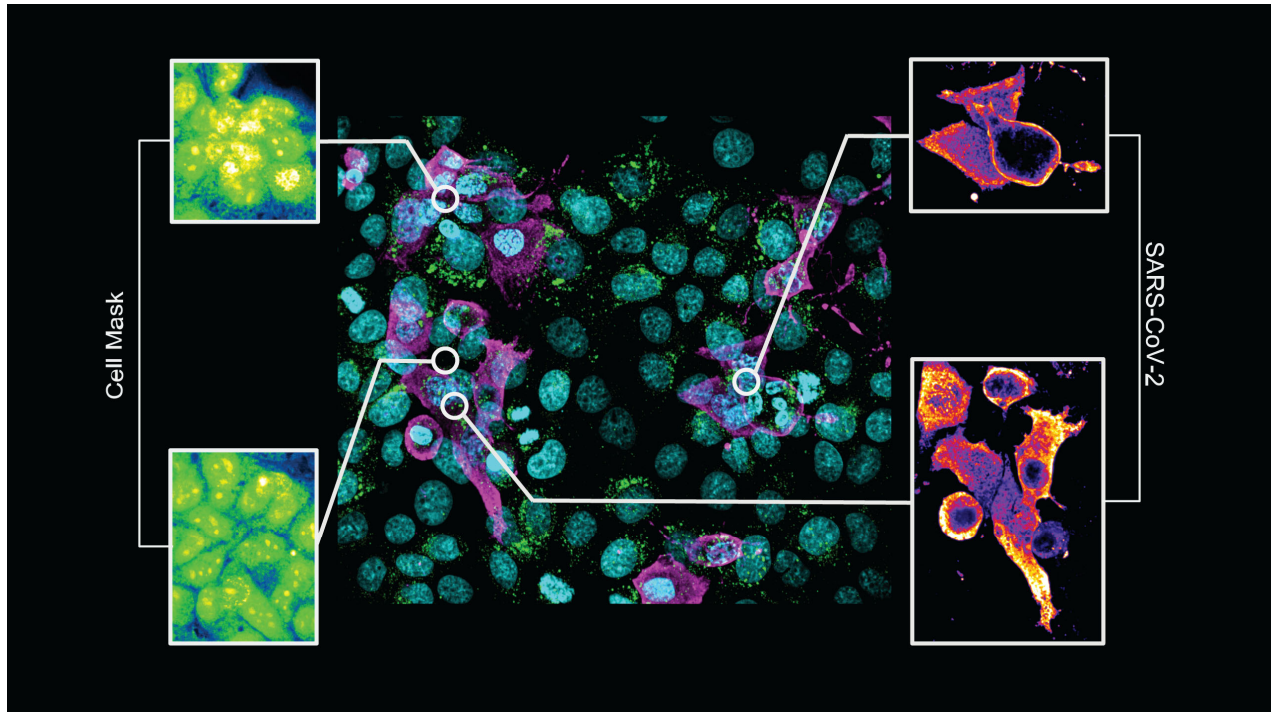
575

576

577

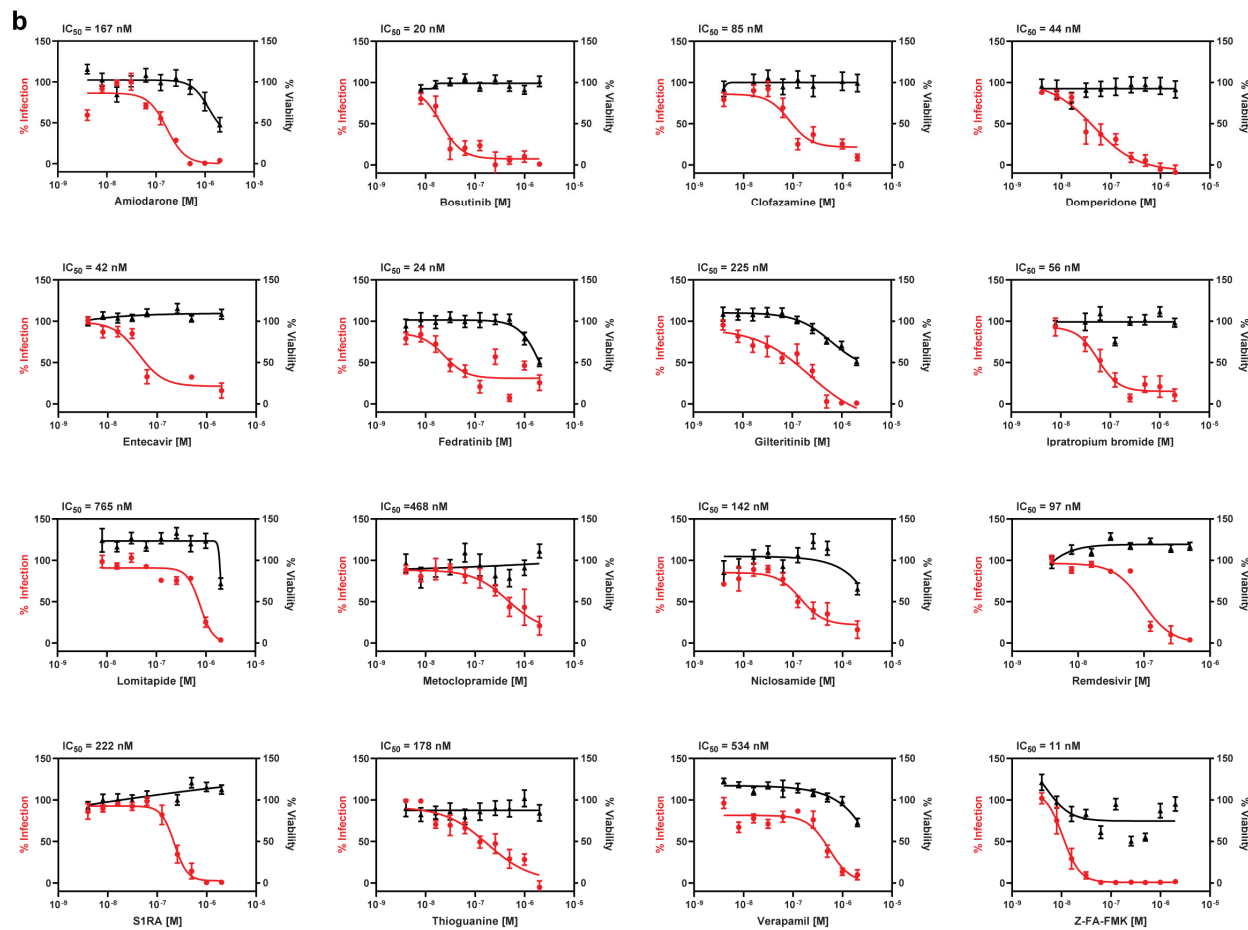
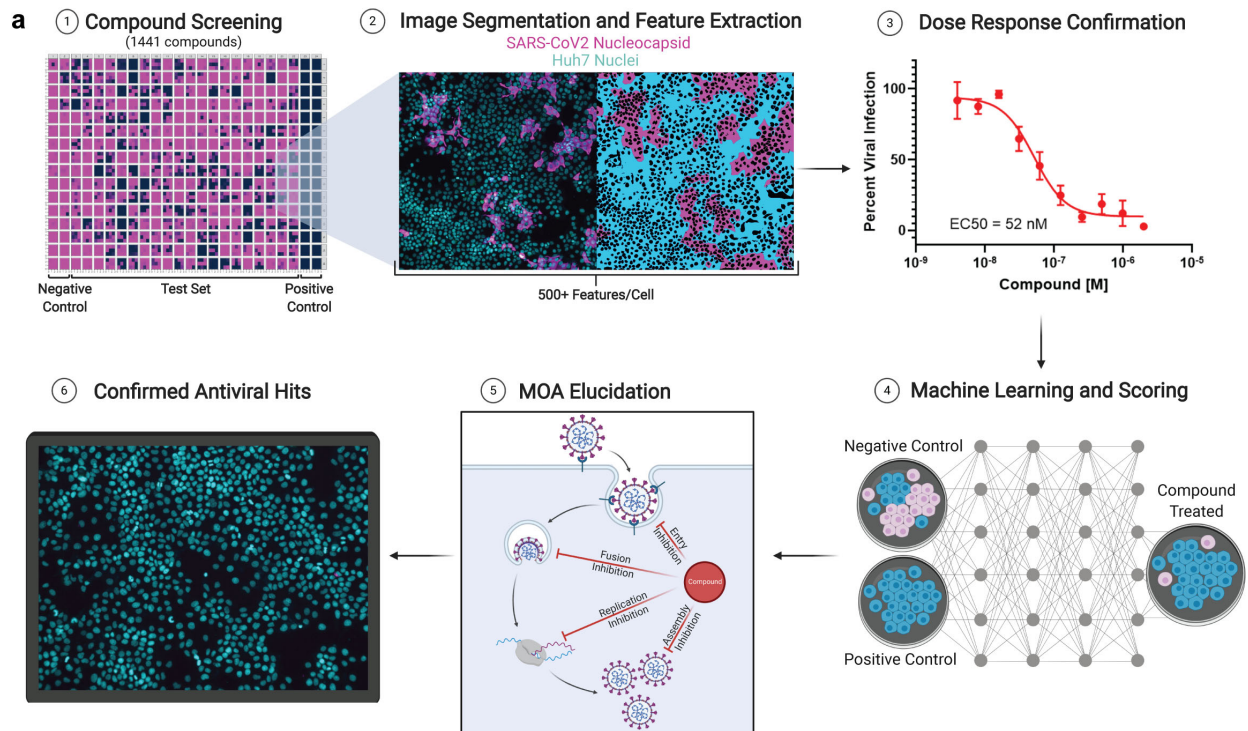
578

579 **FIGURES AND LEGENDS**

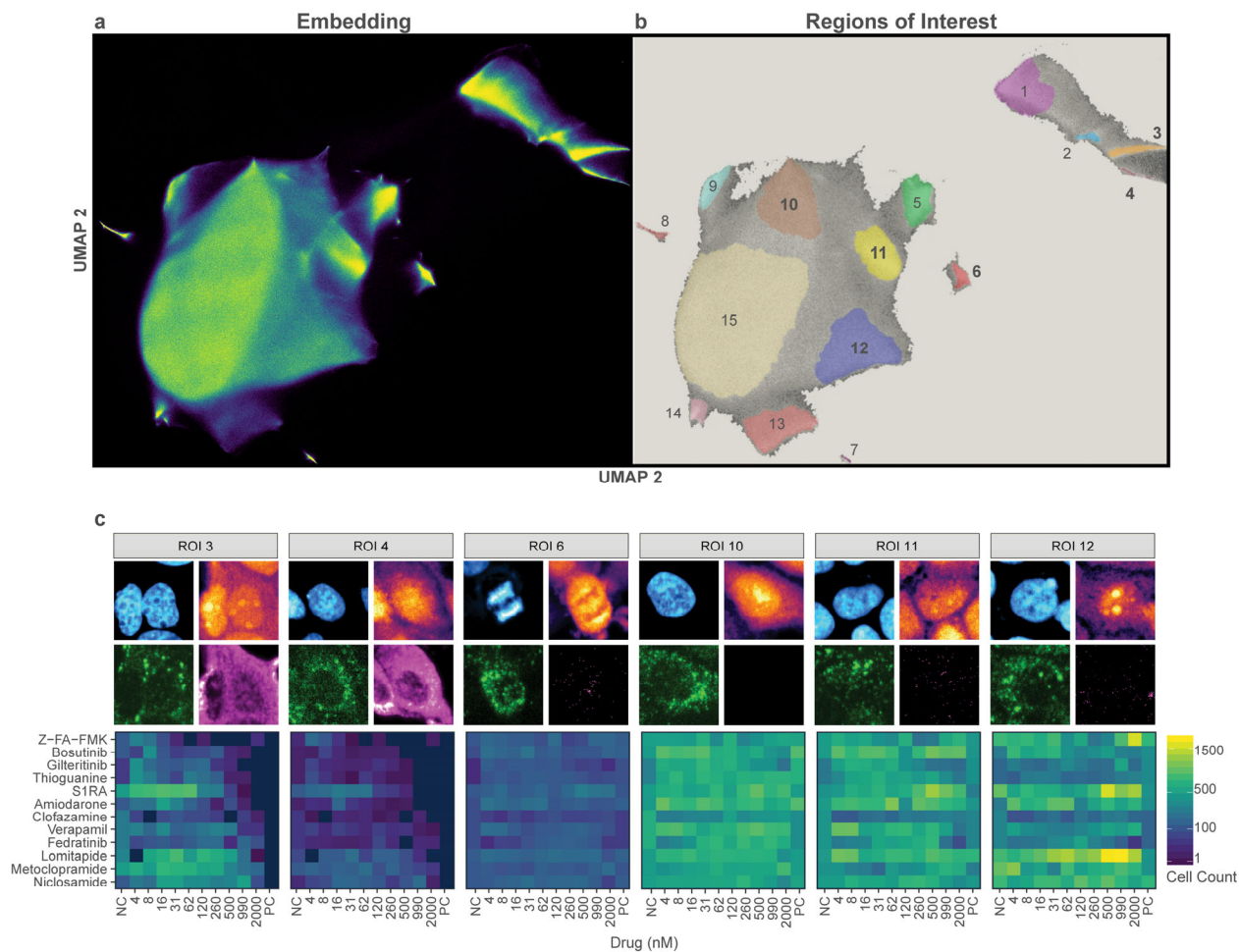


580

581 **Figure 1.** Morphological profiling of SARS-CoV-2 infected Huh7 cells (MOI of 0.2 for 48 hrs).
582 Center image: representative field with nuclei (cyan), neutral lipids (green), and SARS-CoV-2 NP
583 (magenta). Through feature extraction key traits of SARS-CoV-2 infection were characterized with
584 multinucleated syncytia (top left) and abundant nucleoli (bottom left) from HCS CellMask Orange
585 channel. Cell viral compartmentalization (top right) with cytoplasmic protrusions (bottom right)
586 from SARS-CoV-2 NP channel. Representative image was acquired on a Yokogawa CQ1 high-
587 content imager and visualized with Fiji ImageJ package.



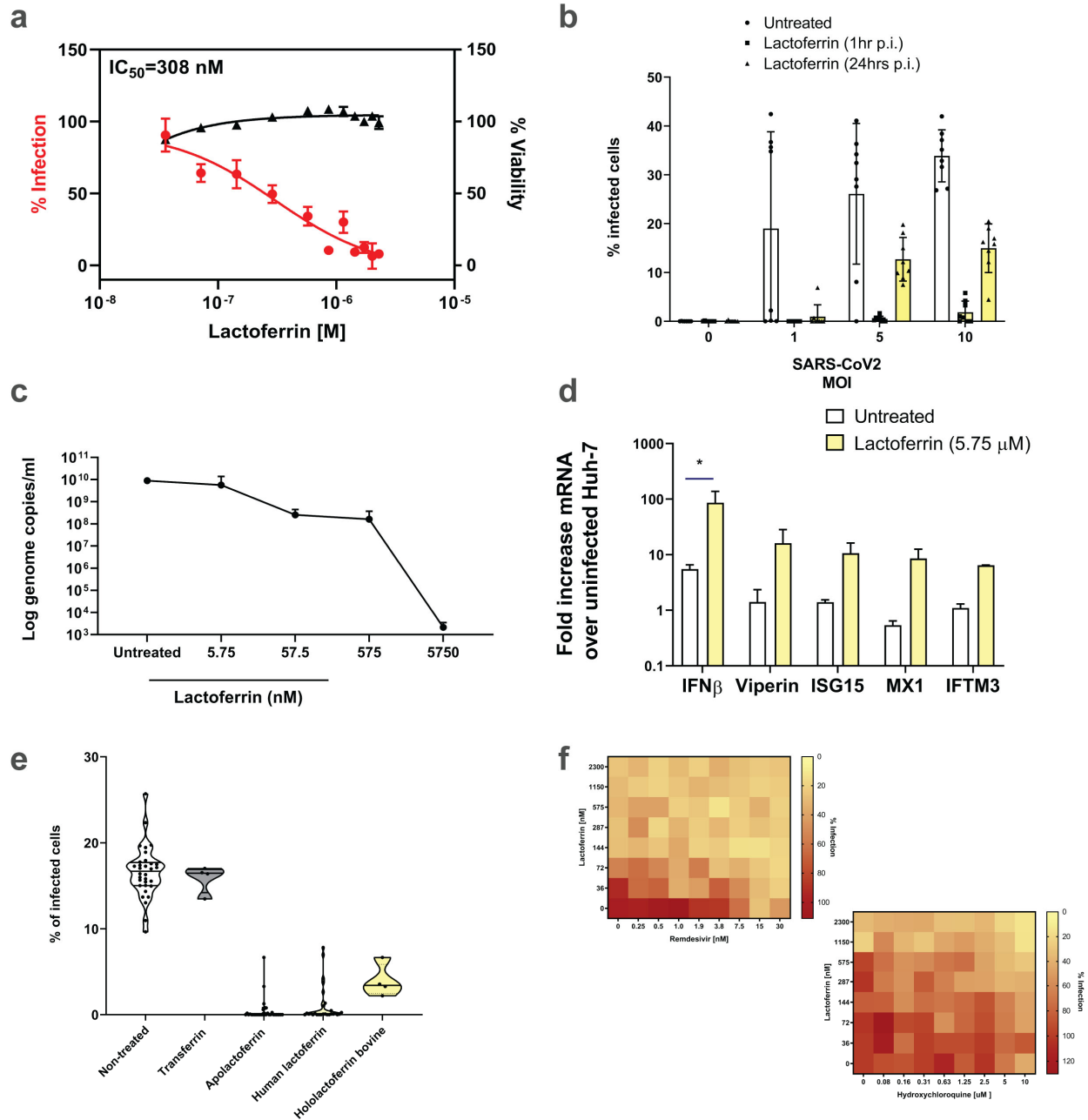
589 **Figure 2.** a) Schematic representation of the anti-SARS-CoV-2 therapy discovery effort. 1)
590 Compounds are administered to cells cultured on 384-well plates infected with SARS-CoV-2.
591 Each plate contains 24 negative (infected) and 24 positive (non-infected) control wells to adjust
592 for plate-to-plate variation. 2) Cells are fixed, stained, and imaged. Images are analyzed through
593 a Cell Profiler-based pipeline which segments nuclei, cell boundaries, neutral lipid content and
594 viral syncytia formation while extracting features of these cellular compartments. 3) Dose-
595 response curves are calculated through multivariate-analysis to define per-image viral infectivity
596 4) Machine learning models are built around positive and negative control wells based on
597 extracted features and applied to each drug condition. 5) Models inform on individual compound
598 mode(s) of antiviral action through obtained features 6) confirmed antiviral hits; b) Dose-response
599 curves of 16 hits of the drug screening. Graphs represent median SEM of 10-point 1:2 dilution
600 series of selected compounds for N=3 biological replicates. IC₅₀ were calculated based on
601 normalization to the control and after fitting in GraphPad Prism.
602



603
 604 **Figure 3.** a) 2 dimensional UMAP embedding of two million individual cells by 379 morphological
 605 features consisting of uninfected (PC), infected (NC), or infected and treated with 12 FDA
 606 approved and clinical candidate drug screening hits across 10 doses. b) Cluster regions of interest
 607 (ROI) in the UMAP are highlighted including infected syncytial (ROI 3) and isolated (ROI 4) cells
 608 and non-infected mitotic (ROI 6), normal (ROI 10), scattered lipid (ROI 11), and cytoplasm
 609 punctate (ROI 12) cells. c) For six ROIs, a representative cell is shown by nuclear (upper-left),
 610 cell boundary (upper-right), neutral lipid (lower-left), and SARS-CoV-2 NP (lower-right) channels.
 611 Below, the cell count across each treatment and dose is shown as a heat-map, where the dose-
 612 responsive behavior for ROIs 3 and 4 are visible.

613

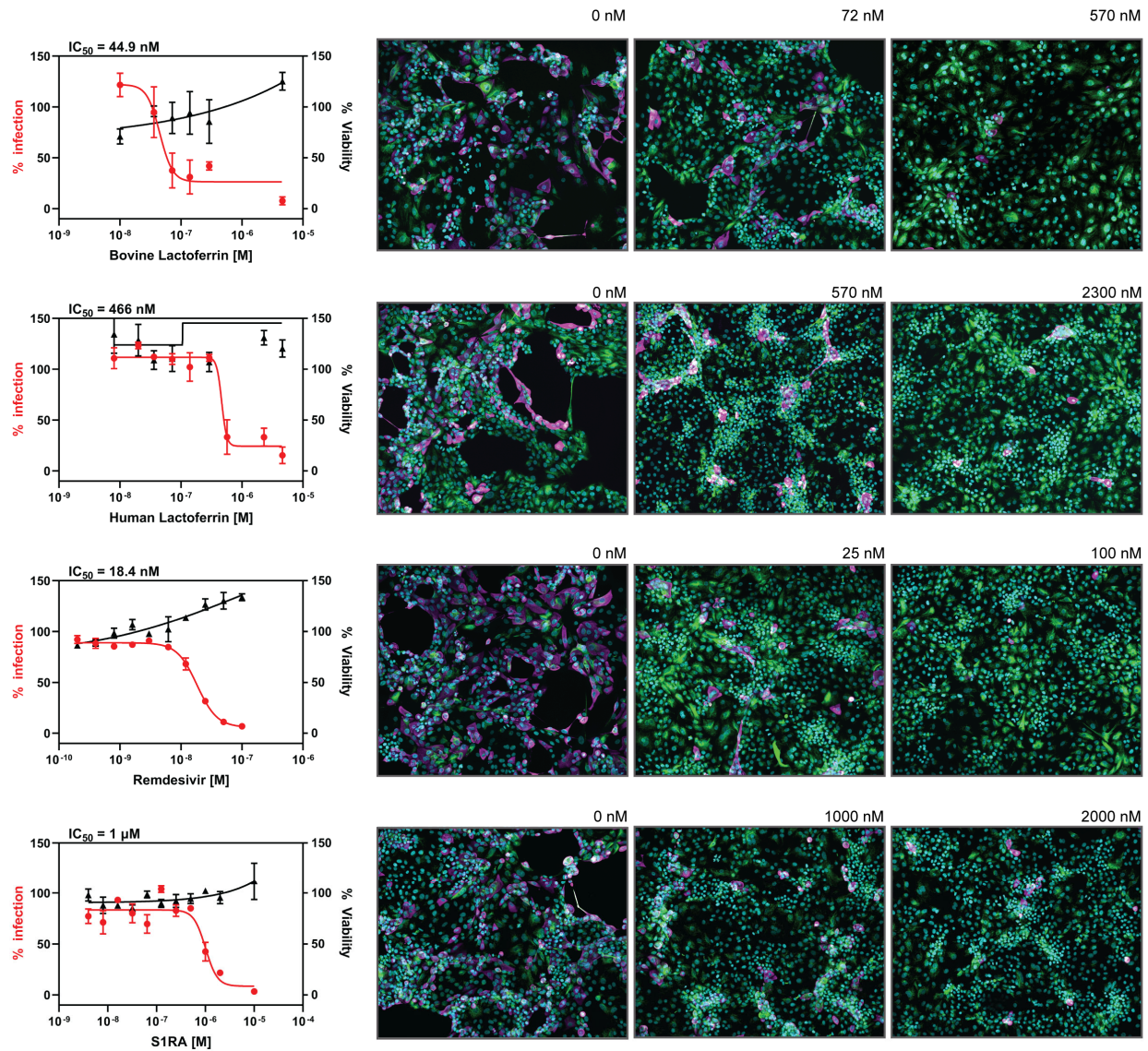
614



615

616 **Figure 4.** Lactoferrin blocks SARS-CoV-2 replication at different stages of the viral cycle. a) Huh7
 617 cells were treated with lactoferrin (0 to 2.3 μ M) and infected with SARS-CoV-2 (MOI of 0.2) in a
 618 384-well plate. Plates were imaged using automated fluorescence microscopy and processed
 619 using our image analysis pipeline to determine percent viral inhibition. Graph indicates a dose-
 620 response (RED, IC_{50} = 308 μ M). Cell viability is depicted in black. b) Huh7 were infected with
 621 SARS-CoV-2 (MOI of 1, 5 and 10; MOI of 0 indicates non-infected cells) and treated with 2.3 μ M

622 of lactoferrin at 1 and 24 hrs p.i. Bars indicate the percentage of infected cells in different
623 conditions. Data is an average of eight replicates. Statistical significance determined using
624 multiple student's t-test with the Bonferroni-Dunn method, with alpha = 0.05. Except for MOI of 0,
625 all conditions (Untreated vs Lactoferrin, 1 hr or Untreated vs Lactoferrin, 24 hr) differ at $P < 0.0001$.
626 c-d) 2.5×10^4 Huh7 cells were infected with SARS-CoV-2 at MOI of 0.2. 48 hrs p.i., cells were
627 harvested and RNA was extracted. Viral genome copies were calculated with an absolute
628 quantification method (standard curve) (c) and mRNA levels of cellular IFN β , MX1, ISG15 and
629 IFITM3 (d) were calculated with $\Delta\Delta C_t$ over non-infected Huh7. Data are average, SD of N=2
630 biological replicates with n=3 technical replicates each. Statistical significance determined using
631 multiple student's t-test with the Bonferroni-Dunn method, with alpha = 0.05. * $P < 0.001$. e)
632 Percentage of SARS-CoV-2 infected Huh7 cells upon treatment with bovine apolactoferrin and
633 hololactoferrin, native human lactoferrin and transferrin at a concentration of 2.3 μM . f) 2-
634 dimensional dose response heat maps of lactoferrin (0 to 2.3 μM) in combination with remdesivir
635 and hydroxychloroquine (0 to 30 nM and 0 to 10 μM , respectively). Remdesivir combination was
636 evaluated with a 0.2 MOI and HCQ was evaluated with a MOI of 10 leading to a relative shift in
637 lactoferrin potency.



638

639 **Figure 5.** Antiviral activity of selected compounds was assessed in iAEC2 cells infected with
640 SARS-CoV-2 at MOI 10. Bovine and human lactoferrin exhibited IC_{50} of 44.9 and 466 nM
641 respectively. Remdesivir and S1RA exhibited IC_{50} of 18.4 nM and 1 μ M respectively. Images of
642 nuclei (cyan), acetylated tubulin (green), and NP (magenta) from non-treated infected control,
643 IC_{50} , and IC_{max} .

644

645

646

647 **SUPPLEMENTARY INFORMATION**

648 Supplementary Figure 1: Screening assay optimization

649 Supplementary Figure 2: Compounds exacerbating SARS-CoV2 infection

650 Supplementary Figure 3: Features of UMAP regions of interest (ROI)

651 Supplementary Figure 4: Combinatory effects of remdesivir and hydroxychloroquine with
652 lactoferrin

653 Supplementary Table 1: Compound Deep Dives

654 Supplementary File 1: Compound library details

655 Supplementary File 2: 3D reconstruction video of infected cells

656

657 **REFERENCES**

658 1. Xiao, F. *et al.* Evidence for Gastrointestinal Infection of SARS-CoV-2. *Gastroenterology*

659 (2020). doi:10.1053/j.gastro.2020.02.055

660 2. Lin, L. *et al.* Gastrointestinal symptoms of 95 cases with SARS-CoV-2 infection. *Gut*

661 (2020). doi:10.1136/gutjnl-2020-321013

662 3. Avula, A. *et al.* COVID-19 presenting as stroke. *Brain. Behav. Immun.* (2020).

663 doi:10.1016/j.bbi.2020.04.077

664 4. Kochi, A. N., Tagliari, A. P., Forleo, G. B., Fassini, G. M. & Tondo, C. Cardiac and

665 arrhythmic complications in patients with COVID-19. *Journal of Cardiovascular*

666 *Electrophysiology* (2020). doi:10.1111/jce.14479

667 5. Mulangu, S. *et al.* A randomized, controlled trial of Ebola virus disease therapeutics. *N.*

668 *Engl. J. Med.* (2019). doi:10.1056/NEJMoa1910993

669 6. Oprea, T. I. *et al.* Drug repurposing from an academic perspective. *Drug Discovery*

670 *Today: Therapeutic Strategies* (2011). doi:10.1016/j.ddstr.2011.10.002

671 7. Chu, H. *et al.* Comparative tropism, replication kinetics, and cell damage profiling of

672 SARS-CoV-2 and SARS-CoV with implications for clinical manifestations, transmissibility,

- 673 and laboratory studies of COVID-19: an observational study. *The Lancet Microbe* (2020).
674 doi:10.1016/s2666-5247(20)30004-5
- 675 8. Hoffmann, M. *et al.* SARS-CoV-2 Cell Entry Depends on ACE2 and TMPRSS2 and Is
676 Blocked by a Clinically Proven Protease Inhibitor. *Cell* (2020).
677 doi:10.1016/j.cell.2020.02.052
- 678 9. Riva, L. *et al.* A Large-scale Drug Repositioning Survey for SARS-CoV-2 Antivirals.
679 *bioRxiv* (2020). doi:10.1101/2020.04.16.044016
- 680 10. Katie Heiser *et al.* Identification of potential treatments for COVID-19 through artificial
681 intelligence enabled phenomic analysis of human cells infected with SARS-CoV-2.
682 *bioRxiv* (2020). doi:10.1101/2020.04.21.054387
- 683 11. Jeon, S. *et al.* Identification of antiviral drug candidates against SARS-CoV-2 from FDA-
684 approved drugs. *Antimicrob. Agents Chemother.* (2020). doi:10.1128/AAC.00819-20
- 685 12. McInnes, L., Healy, J., Saul, N. & Großberger, L. UMAP: Uniform Manifold Approximation
686 and Projection. *J. Open Source Softw.* (2018). doi:10.21105/joss.00861
- 687 13. Lang, J. *et al.* Inhibition of SARS pseudovirus cell entry by lactoferrin binding to heparan
688 sulfate proteoglycans. *PLoS One* (2011). doi:10.1371/journal.pone.0023710
- 689 14. Kell, D. B., Heyden, E. L. & Pretorius, E. The Biology of Lactoferrin, an Iron-Binding
690 Protein That Can Help Defend Against Viruses and Bacteria . *Frontiers in Immunology*
691 **11**, 1221 (2020).
- 692 15. Siqueiros-Cendón, T. *et al.* Immunomodulatory effects of lactoferrin. *Acta*
693 *Pharmacologica Sinica* (2014). doi:10.1038/aps.2013.200
- 694 16. Yeni, P. Update on HAART in HIV. in *Journal of Hepatology* (2006).
695 doi:10.1016/j.jhep.2005.11.021
- 696 17. Hurley, K. *et al.* Reconstructed Single-Cell Fate Trajectories Define Lineage Plasticity
697 Windows during Differentiation of Human PSC-Derived Distal Lung Progenitors. *Cell*
698 *Stem Cell* (2020). doi:10.1016/j.stem.2019.12.009

- 699 18. Jacob, A. *et al.* Derivation of self-renewing lung alveolar epithelial type II cells from
700 human pluripotent stem cells. *Nat. Protoc.* (2019). doi:10.1038/s41596-019-0220-0
- 701 19. Mason, R. J. Pathogenesis of COVID-19 from a cell biology perspective. *European*
702 *Respiratory Journal* (2020). doi:10.1183/13993003.00607-2020
- 703 20. Evans, W. E. Pharmacogenetics of Thiopurine S-Methyltransferase and Thiopurine
704 Therapy. in *Therapeutic Drug Monitoring* (2004). doi:10.1097/00007691-200404000-
705 00018
- 706 21. Arbiser, J. L. & Moschella, S. L. Clofazimine: A review of its medical uses and
707 mechanisms of action. *Journal of the American Academy of Dermatology* (1995).
708 doi:10.1016/0190-9622(95)90134-5
- 709 22. Alghamdi, S., Leoncikis, V., Plant, K. E. & Plant, N. J. Synergistic interaction between
710 lipid-loading and doxorubicin exposure in Huh7 hepatoma cells results in enhanced
711 cytotoxicity and cellular oxidative stress: Implications for acute and chronic care of obese
712 cancer patients. *Toxicol. Res. (Camb)*. (2015). doi:10.1039/c5tx00173k
- 713 23. Hibbs, A. M. & Lorch, S. A. Metoclopramide for the treatment of gastroesophageal reflux
714 disease in infants: A systematic review. *Pediatrics* (2006). doi:10.1542/peds.2005-2664
- 715 24. Hajifathalian, K. *et al.* SARS-COV-2 infection (coronavirus disease 2019) for the
716 gastrointestinal consultant. *World J. Gastroenterol.* (2020). doi:10.3748/wjg.v26.i14.1546
- 717 25. Roscow, O., Ganassin, R., Garver, K. & Polinski, M. Z-FA-FMK demonstrates differential
718 inhibition of aquatic orthoreovirus (PRV), aquareovirus (CSRV), and rhabdovirus (IHNV)
719 replication. *Virus Res.* (2018). doi:10.1016/j.virusres.2017.11.024
- 720 26. Ou, X. *et al.* Characterization of spike glycoprotein of SARS-CoV-2 on virus entry and its
721 immune cross-reactivity with SARS-CoV. *Nat. Commun.* (2020). doi:10.1038/s41467-
722 020-15562-9
- 723 27. Pardanani, A. *et al.* TG101209, a small molecule JAK2-selective kinase inhibitor potently
724 inhibits myeloproliferative disorder-associated JAK2V617F and MPLW515L/K mutations.

- 725 *Leukemia* (2007). doi:10.1038/sj.leu.2404750
- 726 28. Wu, D. & Yang, X. O. TH17 responses in cytokine storm of COVID-19: An emerging
727 target of JAK2 inhibitor Fedratinib. *J. Microbiol. Immunol. Infect.* (2020).
728 doi:10.1016/j.jmii.2020.03.005
- 729 29. Zhang, W. *et al.* The use of anti-inflammatory drugs in the treatment of people with
730 severe coronavirus disease 2019 (COVID-19): The experience of clinical immunologists
731 from China. *Clinical Immunology* (2020). doi:10.1016/j.clim.2020.108393
- 732 30. Stebbing, J. *et al.* COVID-19: combining antiviral and anti-inflammatory treatments. *The*
733 *Lancet Infectious Diseases* (2020). doi:10.1016/S1473-3099(20)30132-8
- 734 31. Treatment of Moderate to Severe Coronavirus Disease (COVID-19) in Hospitalized
735 Patients. (2020). Available at: <https://clinicaltrials.gov/ct2/show/NCT04321993>.
- 736 32. Delprat, B., Crouzier, L., Su, T. P. & Maurice, T. At the Crossing of ER Stress and MAMs:
737 A Key Role of Sigma-1 Receptor? in *Advances in Experimental Medicine and Biology*
738 (2020). doi:10.1007/978-3-030-12457-1_28
- 739 33. Friesland, M., Mingorance, L., Chung, J., Chisari, F. V. & Gastaminza, P. Sigma-1
740 Receptor Regulates Early Steps of Viral RNA Replication at the Onset of Hepatitis C
741 Virus Infection. *J. Virol.* (2013). doi:10.1128/jvi.03557-12
- 742 34. Fung, T. S. & Liu, D. X. Coronavirus infection, ER stress, apoptosis and innate immunity.
743 *Frontiers in Microbiology* (2014). doi:10.3389/fmicb.2014.00296
- 744 35. Moebius, F. F., Reiter, R. J., Hanner, M. & Glossmann, H. High affinity of sigma1-binding
745 sites for sterol isomerization inhibitors: Evidence for a pharmacological relationship with
746 the yeast sterol C8-C7 isomerase. *Br. J. Pharmacol.* (1997). doi:10.1038/sj.bjp.0701079
- 747 36. Díaz, J. L. *et al.* Synthesis and biological evaluation of the 1-arylpyrazole class of σ 1
748 receptor antagonists: Identification of 4-{2-[5-methyl-1-(naphthalen-2-yl)-1H-pyrazol-3-
749 yloxy]ethyl}morpholine (S1RA, E-52862). *J. Med. Chem.* (2012). doi:10.1021/jm3007323
- 750 37. Torres, V. *et al.* QT prolongation and the antiarrhythmic efficacy of amiodarone. *J. Am.*

- 751 *Coll. Cardiol.* (1986). doi:10.1016/S0735-1097(86)80272-8
- 752 38. Vidal-Torres, A. *et al.* Effects of the selective sigma-1 receptor antagonist S1RA on
753 formalin-induced pain behavior and neurotransmitter release in the spinal cord in rats. *J.*
754 *Neurochem.* (2014). doi:10.1111/jnc.12648
- 755 39. Gris, G. *et al.* The selective sigma-1 receptor antagonist E-52862 attenuates neuropathic
756 pain of different aetiology in rats. *Sci. Rep.* (2016). doi:10.1038/srep24591
- 757 40. Gordon, D. E. *et al.* A SARS-CoV-2 protein interaction map reveals targets for drug
758 repurposing. *Nature* (2020). doi:10.1038/s41586-020-2286-9
- 759 41. Reghunathan, R. *et al.* Expression profile of immune response genes in patients with
760 severe acute respiratory syndrome. *BMC Immunol.* (2005). doi:10.1186/1471-2172-6-2
- 761 42. Cutone, A. *et al.* Lactoferrin prevents LPS-induced decrease of the iron exporter
762 ferroportin in human monocytes/macrophages. *BioMetals* (2014). doi:10.1007/s10534-
763 014-9742-7
- 764 43. Conti, P. *et al.* Induction of pro-inflammatory cytokines (IL-1 and IL-6) and lung
765 inflammation by COVID-19: anti-inflammatory strategies. *Journal of biological regulators*
766 *and homeostatic agents* (2020). doi:10.23812/CONTI-E.
- 767 44. Lagunas-Rangel, F. A. & Chávez-Valencia, V. High IL-6/IFN- γ ratio could be associated
768 with severe disease in COVID-19 patients. *Journal of Medical Virology* (2020).
769 doi:10.1002/jmv.25900
- 770 45. Han, C. *et al.* Digestive Symptoms in COVID-19 Patients With Mild Disease Severity:
771 Clinical Presentation, Stool Viral RNA Testing, and Outcomes. *Am. J. Gastroenterol.*
772 (2020). doi:10.14309/ajg.0000000000000664
- 773 46. Oda, H. *et al.* Antiviral Effects of Bovine Lactoferrin on Human Norovirus. *Biochem. Cell*
774 *Biol.* (2020). doi:10.1139/bcb-2020-0035
- 775 47. Mohamed, J. A. *et al.* A Novel Single-Nucleotide Polymorphism in the Lactoferrin Gene Is
776 Associated with Susceptibility to Diarrhea in North American Travelers to Mexico. *Clin.*

- 777 *Infect. Dis.* (2007). doi:10.1086/512199
- 778 48. Gu, J., Han, B. & Wang, J. COVID-19: Gastrointestinal Manifestations and Potential
779 Fecal–Oral Transmission. *Gastroenterology* (2020). doi:10.1053/j.gastro.2020.02.054
- 780 49. Hung, I. F.-N. *et al.* Triple combination of interferon beta-1b, lopinavir–ritonavir, and
781 ribavirin in the treatment of patients admitted to hospital with COVID-19: an open-label,
782 randomised, phase 2 trial. *Lancet* (2020). doi:10.1016/s0140-6736(20)31042-4
- 783 50. Berthold, M. R. *et al.* KNIME: The konstanz information miner. in *4th International*
784 *Industrial Simulation Conference 2006, ISC 2006* (2006). doi:10.1145/1656274.1656280
- 785 51. Stevens, J.-L., Rudiger, P. & Bednar, J. HoloViews: Building Complex Visualizations
786 Easily for Reproducible Science. in *Proceedings of the 14th Python in Science*
787 *Conference* (2015). doi:10.25080/majora-7b98e3ed-00a
- 788